RESEARCH ARTICLE
PLANETARY SCIENCES

Earth and Planetary Physics
10: 337–348, 2026
doi: 10.26464/epp2026029

Research on imaging detection technology for 10–100 keV medium-energy electrons

JiaChen Sun[1†], YuGuang Ye[2†], Hong Zou[1,2*], JiaLi Chen[1], TianHao Li[1], and WeiHong Shi[1]

[1]School of Earth and Space Sciences, Peking University, Beijing 100871, China;

[2]State Key Laboratory of Lunar and Planetary Sciences, Macao University of Science and Technology, China National Space Administration (CNSA) Macao Center for Space Exploration and Science, Macao 999078, China

Key Points:

- A cross-type imaging electron spectrometer is used to achieve quasi-three-dimensional imaging observations of incident electrons.
- The lower energy boundary of the detector is extended to ~10 keV by improving the silicon detector and amplification system.
- The new imaging spectrometer is able to perform high temporal, spatial, and energy resolution imaging detection of 10–100 keV electrons in the magnetosphere.

Citation: Sun, J. C., Ye, Y. G., Zou, H., Chen, J. L., Li, T. H., and Shi, W. H. (2026). Research on imaging detection technology for 10–100 keV medium-energy electrons. *Earth Planet. Phys.*, *10*(2), 337–348. http://doi.org/10.26464/epp2026029

Abstract: Electrons in the energy range of 10–100 keV are important energetic particle components in the magnetosphere, and they play a key role in many physical processes in the magnetosphere. However, many scientific questions about these processes are still unanswered. High spatiotemporal and energy-resolution imaging detection of 10–100 keV electrons is of great significance for solving these scientific problems. The traditional space particle detection technology cannot effectively detect the medium-energy electrons in this energy range. In this project, we propose combining low-noise particle detection technology with pinhole imaging technology to achieve high-resolution imaging detection of 10–100 keV medium-energy electrons in the magnetosphere, and at the same time achieve miniaturization (≤3.2 kg and size of 150 × 150 × 170 mm) and low power consumption (≤5 W) of the instrument, which can be used for space physics research and space weather applications in the future.

Keywords: 10–100 keV; medium-energy electrons; quasi-three-dimensional imaging detection; imaging electron spectrometer; continuous spectrum

1. Introduction

The heliosphere, as we know, is filled with space plasma composed of electrons, protons, and other heavy ions at varying energies. Within the planetary magnetospheres, the energy range of space plasma typically spans from sub electron volts (eV) to several hundred kilo electron volts (keV), occasionally reaching tens of megaelectron volts (MeV). Electrons within 10 keV to 100 keV are called medium-energy electrons in magnetospheric physics research (Kasahara et al., 2018). Although their flux is lower than that of low-energy electrons, they constitute a significant energetic particle component within the magnetosphere, playing a pivotal role in physical processes. During geomagnetic activity, processes such as magnetic reconnections in the magnetotail accelerate and transport medium-energy electrons from the magnetotail into the inner magnetosphere, generating substorm energy electron injections (Zong QG et al., 2016; Liu ZY et al., 2018). Subsequently, within the inner magnetosphere, these medium-energy electrons engage in resonant interactions with ultra-low-frequency (ULF) waves and particle drift-bouncing processes (Zong QG et al., 2017; Klimushkin et al., 2021; Zong QG, 2022), which may further accelerate them into radiation belt "killer electrons." Through cyclotron and Landau resonance, they excite very-low-frequency (VLF) whistles (harmonic modes, hiss modes, Z modes, etc.; Summers et al., 1998; Thorne, 2010; Thorne et al., 2013). These particles scatter pitch angle through interaction with VLF waves, precipitating into the polar ionosphere and upper atmosphere to generate auroras. However, some questions remain unresolved. We need deeper insights into the nonlinear drift-resonance interaction between ULF waves and energetic electrons, the excitation mechanisms of VLF waves and their cyclotron-resonance nonlinear interactions with energetic electrons, auroral particle precipitation, and aurora formation. The present understanding of the contributions of ULF and VLF waves (such as whistle-mode waves) to electron acceleration in radiation belts remains incomplete. Resolving these questions relies on better observations of medium-energy electrons. Beyond planetary magnetospheres, electrons within 10 keV to 100 keV also

† Co-first authors: J. C. Sun, space_sunjiachen@stu.pku.edu.cn
Y.G. Ye, ygye@must.edu.mo
Correspondence to: H. Zou, hongzou@pku.edu.cn
Received 24 OCT 2025; Accepted 17 JAN 2026.
First Published online 29 JAN 2026.

constitute a significant component of interplanetary solar wind plasma as suprathermal electrons (Luhmann et al., 2008). They constitute primary particle species in solar energetic particle events, which is the most frequent solar burst activity. Observations of solar energetic particle events and their energy spectra can provide information about the locations of burst source regions, facilitating studies of electron acceleration and transport (Lin RP et al., 2008).

Although the detection of electrons in the several kilo electron volt to 100 keV range is important for space physics research, conventional particle detection techniques have difficulty observing electrons across this entire energy range by using a single instrument. The measurement of electrons with energy below 30 keV generally falls within the scope of plasma detection and is typically achieved using electrostatic deflection systems coupled with microchannel plates (MCPs) or channel electron multipliers (CEMs). Classic electrostatic analyzers (ESAs) include the three-dimensional (3D) Plasma and Energetic Particle Instrument on the Wind spacecraft (Lin RP et al., 1996) and the ElectroStatic Analyzer on the Time History of Events and Macroscale Interactions during Substorms (THEMIS) spacecrafts (McFadden et al., 2009). In such analyzers, electrons enter through the top hat aperture and are subjected to an electric field between concentric hemispherical structures. Only electrons with specific energies can pass the hemispheres and reach the MCP detector at the bottom. The energy of electrons that reach the detector is determined by the voltage applied to the hemispherical electrodes. By varying this voltage, measurements of electrons at different energy levels can be obtained. The top hat allows electrons to enter from a 360° azimuthal range. Multiple anodes form a designated number of sectors, enhancing the instrument's azimuthal resolution, so top hat ESAs can provide high spatial resolution observations. However, because of limitations in the maximum voltage of the stepped high-voltage power and the efficiency of the MCP detectors, the maximum measured energy in conventional top hat ESAs is typically around 30 keV. For instance, the maximum measured energy of the THEMIS top hat ESA is approximately 32 keV. Additionally, ESAs use a stepped high-voltage sweep to scan energy. The instrument must maintain each voltage step for a period (usually several milliseconds). Because completing a voltage sweep takes time, electrons of different energies are measured at different times; thus, the temporal resolution of electron measurements with ESAs is inherently limited.

In conventional particle detection techniques, high-energy electron detection is typically achieved using solid-state detectors. However, limited by sensor performance and system electronics noise, solid-state detectors can generally only measure electrons with energy above 30 keV. A typical medium-energy electron detector is the Medium Energy Proton Electron Detector (MEPED) within the Space Environment Monitor suite aboard the National Oceanic and Atmospheric Administration's (NOAA's) polar-orbiting meteorological satellites (Evans and Greer, 2000). The MEPED comprises two orthogonally arranged electron probes and an electronic box. Each probe utilizes a telescope consisting of a passive collimator coupled with a 700-μm-thick silicon semiconductor detector. Owing to its relatively simple electronics and limited telemetry, the MEPED provides coarse measurements with just three integral energy bins (E1: >30 keV; E2: >100 keV; and E3: >300 keV), thus precluding a refined electron spectrum. Another type of electron spectrometer utilizes the pinhole imaging principle to simultaneously observe medium-energy electron spectra in multiple directions. By utilizing more modern multipixel silicon detectors and integrated preamplifier Application-Specific Integrated Circuit (ASIC) technology, such electron spectrometers typically achieve a lower energy boundary of 20–50 keV (Blake et al., 1995; Wilken et al., 1997; Zou H et al., 2018; Ye YG et al., 2021, 2023b).

Both of the above-mentioned techniques have difficulty with measurement accuracy at the boundaries of their energy ranges. Moreover, because of the differences in measurement principles, it is difficult to align their measurement, especially when close to the energy boundary (Kasahara et al., 2018). Therefore, continuous observation of medium-energy electrons in the energy range of 10 to 100 keV remains a challenge.

Instrument scientists have attempted to address these technical challenges by refining both of these typical particle detector technologies. Kasahara et al. (2018) enhanced the conventional ESA to extend the upper boundary of electron energy measurable by the instrument. Aboard Japan's Exploration of Energization and Radiation in Geospace (ERG) mission, this instrument is known as the Medium-energy Particle Experiments–Electron Analyzer (MEP-e). The MEP-e sensor comprises a Cusp-type ESA and avalanche photodiodes. The ESA determines the energy of incident electrons while excluding ions and photons. The avalanche photodiodes replace conventional electron detectors in ESAs, such as MCPs or CEMs. Microchannel plates or CEMs have low quantum efficiency for electrons above several kilo electron volts, complicating prediction detection efficiency curves for medium-energy electrons. The Cusp-type ESA is specifically engineered for medium-energy electron measurement. Its deflection plates have a curvature center displaced from the probe's symmetry axis, enabling a large curvature radius within compact deflection plate dimensions and thus a broader range of measurable electron energies. Therefore, the MEP-e achieves an electron energy measurement range of 7–87 keV, extending the upper boundary while retaining its imaging capability. However, the MEP-e shares the temporal resolution limitations of conventional ESAs. An energy scan requires 250 milliseconds. Because electrons at different energies cannot be observed simultaneously, this constrains its temporal resolution.

Continuous measurement of electron spectra spanning 10–100 keV has also been achieved by extending the lower energy boundary of solid-state detectors, such as the Suprathermal Electron (STE) instrument aboard the Solar Terrestrial Relations Observatory (STEREO) mission (Lin RP et al., 2008) and the Suprathermal Electrons and Protons (STEP) unit of the Energetic Particle Detector (EPD) aboard the Solar Orbiter mission (Rodríguez et al., 2020). The STE utilizes specially designed silicon semiconductor detectors and readout circuits to extend the lower energy boundary of solid-state electron measurements. It utilizes a four-pixel linear array silicon semiconductor detector featuring an ultra-thin incident window dead layer (Tindall et al., 2008).

Each pixel exhibits a small area and low capacitance and is passively cooled to −30 °C to −90 °C during operation. Additionally, the STE uses a readout electronics system composed of carefully selected discrete components, whose electronic noise is controlled below 1.5 keV after cooling. With these improvements, the STE achieves superior performance. Using similar principles and technologies as the STE, the STEP unit of the EPD achieves better performance. However, the STE and EPD aim to observe superthermal electrons from the sun, so the instruments are designed for solar particles and cannot conduct imaging observations. Nevertheless, for their technical solutions, the STE and EPD are highly informative.

Recently, imaging detection techniques for medium-energy electrons in the 10–100 keV range have developed considerably. Based on ESA technology, the MEP-e uses a specially designed Cusp-type ESA and avalanche diodes to continuously measure electron energy spectra from 7 to 87 keV. However, the lack of prior data from avalanche diodes limits the use of MEP-e observations. In contrast, the STE detector adopts a different approach. It uses specially designed ultra-thin dead-layer silicon semiconductor detectors and high-performance discrete readout electronics to measure the energy spectrum for electrons ranging from 2 to 100 keV. Nevertheless, the STE requires a low temperature of −30 °C to −90 °C and is specifically engineered for detecting superthermal solar wind electrons and lacks imaging capabilities. To date, no imaging payload has been designed for observing medium-energy electrons (10–100 keV) within the magnetosphere.

This research is based on a prototype of the cross-shaped medium-energy electron imager designed for electron detection in the magnetosphere. With improvements in the original silicon sensor and its amplification system, it covers an energy range from 10 to 100 keV while retaining its imaging detection capability. Section 2 introduces the design and testing of the imager; Section 3 details technical improvements to the imager probe; Section 4 includes the instrument's improved energy response to radioactive sources; and Section 5 concludes with a summary.

2. Principle and Test Results of the Cross-type Imaging Spectrometer

2.1 Principle of Pinhole Imaging Detection

A detailed description of the design and test results of the cross-type imaging electron spectrometer (IES) can be found in Ye YG et al. (2023a). The present study provides only a brief overview of the fundamental principles, circuitry, structural design, and test results pertaining to the cross-type IES as it relates to the design of the suprathermal electron spectrometer.

The design of the cross-type IES is based on the Peking University Imaging Electron Spectrometer (BD-IES) developed by the team at Peking University and deployed aboard China's navigation satellites (Zou H et al., 2018). The BD-IES probe utilizes three linear-array pinhole imaging units to achieve nine-directional energy spectrum measurements of energetic electrons; its structure is illustrated in Figure 1 (Ye YG et al., 2023a). The BD-IES probe structure adopts a design similar to the IES probe on the Cluster mission (Wilken et al., 1997). As shown in Figure 1a, each imaging unit comprises a shielded housing with an aperture, housing a three-element linear array Si-PIN (Positive-Intrinsic-Negative) detector, termed a three-element linear array imaging unit. Each Si-PIN detector and aperture together form an equivalent telescope structure. Each imaging unit can form three telescopes, covering an angular field of approximately 60°. The BD-IES probe, comprising three imaging units, achieves 180° angular coverage, as illustrated in Figure 1b.

The BD-IES probe has a field of view covering a 180° polar angle and a ~30° azimuthal angle. If the BD-IES probe does not rotate along the polar axis, it can only cover a 180° × 30° field of view and cannot achieve a full 3D imaging of incident electrons.

To achieve a 3D imaging observation of incident electrons, we have improved the structure of the BD-IES probe, as shown in

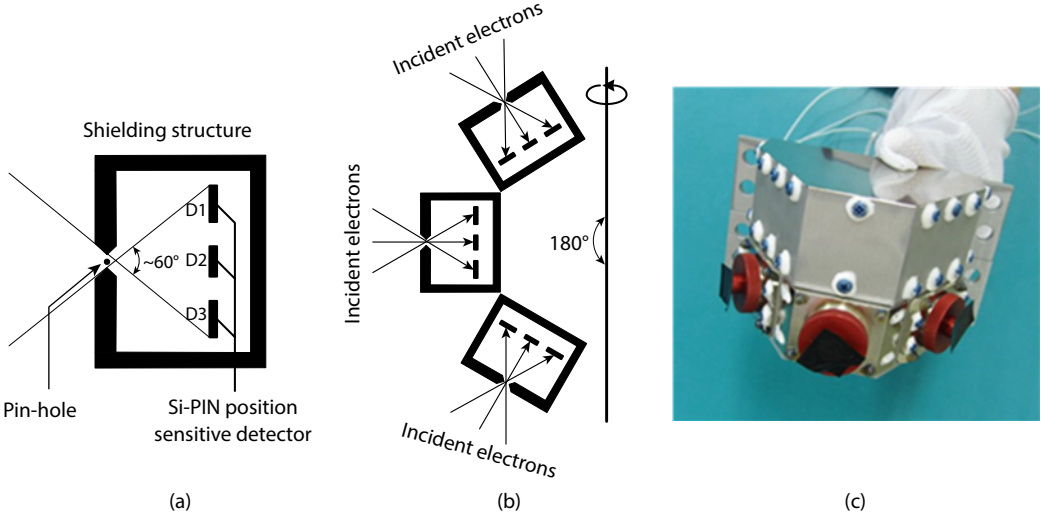

Figure 1. Schematic diagram and photograph of the probe structure of the energy electron imaging system (adopted from Ye YG et al., 2023a). (a) Cross-sectional view of a single detection unit with a detection range of 60°; (b) probe consisting of three detection units, with a measurable polar angle range of 180°; (c) photograph of the probe. D1, D2 and D3 are pixels of the silicon detector.

Figure 2. The specific structural design can be found in Ye YG et al. (2023a). Figure 2 shows the structure of the cross-type energy electron imaging probe. The cross-type energy electron imaging probe has a total of 21 directional telescopes. If these directional telescopes can simultaneously observe incident medium-energy electrons within their respective angular ranges, they can achieve a quasi-3D imaging observation of incident electrons.

2.2 Si-PIN Detectors

Two types of Si-PIN detectors are used in the cross-shaped energy electron imaging probe, both of which were jointly designed by Peking University and the Micron semiconductor company and manufactured by the Micron semiconductor company. In this study, we introduce a three-pixel linear array silicon detector related to the improvement scheme, as shown in Figure 3 (Ye YG et al., 2023a). Figure 3a shows the positive–negative junction surface of the three-pixel linear array silicon detector, which is fabricated using micromachining technology with three symmetrically arranged linear array detector units. Figure 3b shows the ohmic surface of the silicon detector. The ohmic surface of the silicon detector is plated with 2 mm aluminum as the particle incident surface to block photons and low-energy ions.

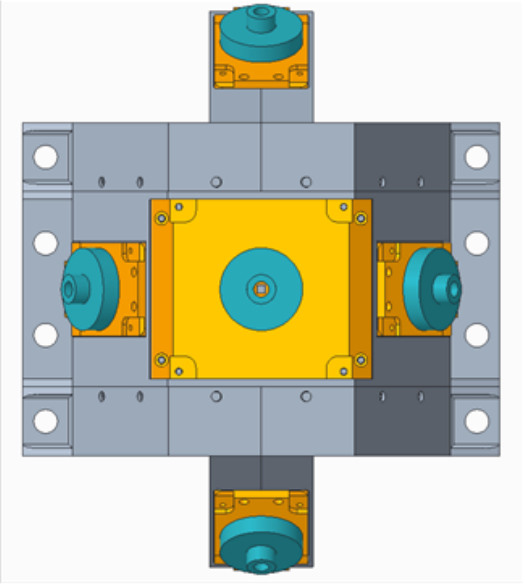

Figure 2. Structural diagram of the cross-type IES probe (adopted from Ye YG et al., 2023a).

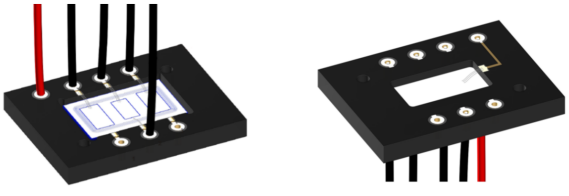

(a) (b)

Figure 3. A three-pixel linear array silicon detector manufactured by the Micron semiconductor company (adopted from Ye YG et al., 2023a). (a) The junction surface of the three-pixel linear array detector; (b) the ohmic surface of the three-pixel linear array detector.

This Si-PIN position-sensitive detector is an advanced ion-implanted silicon detector with a thickness of 1000 μm. This type of detector has low requirements for environmental conditions, making it convenient for storage, testing, and application. Currently, three-pixel linear array silicon detectors have been successfully applied in multiple satellite energy electron detector projects, such as Navigation, Fengyun, and Macao Science Satellite-1 (MSS-1; Zou H et al., 2018; Ye YG et al., 2021, 2023a, b, 2024).

2.3 Readout Circuits

The improvement of the cross-type energy electron imaging probe in this study mainly involves the circuit part from the silicon detector to the preamplifier. Therefore, only the preamplifier-related circuit part of the cross-type energy electron imaging probe is introduced here. The other data processing parts are the same as in the original instrument and can be referred to in the relevant article (Ye YG et al., 2023a).

To minimize system noise, readout circuits that process weak signals from the probe are also integrated into the probe. Each detector unit and readout circuit form a separate signal channel, and the entire cross-shaped energy electron imaging probe has a total of 21 independent channels. We have chosen the RENA-3 (Readout Electronics for Nuclear Applications) chip developed by Novarad, USA. The RENA-3 chip is an event-driven integrated preamplifier that integrates a total of 36 channels. Each channel includes a charge-sensitive amplifier, a shaping circuit, a threshold detection circuit, a peak detection/holding circuit, a trigger, and a series of other front-end electronics. When an incident electron generates a signal in the detector, the corresponding channel of the chip recognizes it as a particle incident event, which in turn drives the subsequent series of circuits to work and complete the collection of information about the event (including the trigger channel number and the peak height of the event pulse). The RENA-3 chip has characteristics such as low noise and a self-reset function (Tumer et al., 2006), and it has been widely used in various space particle detection instruments (Zou H et al., 2018; Ye YG et al., 2021, 2023b, 2024).

Two integrated preamplifier ASIC chips are used to amplify, process, and collect particle signals from the 21 independent channels. In the probe, we designed two identical printed boards (ASIC1 and ASIC2 boards), each of which includes an integrated preamplifier ASIC chip, the power system required by the chip, and the interface with the subsequent data acquisition circuit. Figure 4 shows one ASIC board inside the imaging probe and the assembled probe structure. For a detailed description of the circuitry inside the probe, please refer to the relevant article (Ye YG et al., 2023a).

2.4 Test Results for the Cross-type Medium-Energy IES

For detailed calibration results of the cross-type medium-energy IES, please refer to the relevant article (Ye YG et al., 2023a). In this study, for a performance comparison, the original energy response of a certain three-pixel imaging unit (corresponding to directional channels 13, 15, and 17) of the instrument before being redesigned, to a radioactive source, is briefly introduced.

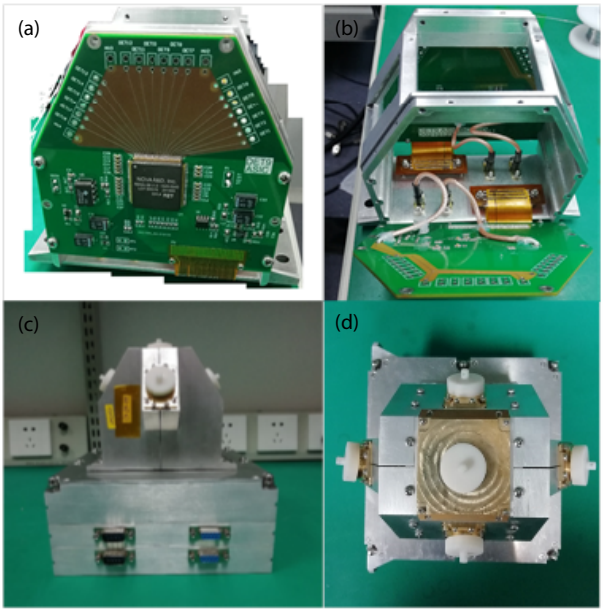

Figure 4. Physical image of the ASIC board (front, back, and interface) in the cross-type energy electron imaging probe and the assembled instrument. (a) Front side of the ASIC board; (b) back side of the ASIC board; (c) side view of the instrument; (d) top view of the instrument.

Figure 5 shows the multichannel energy spectrum of the ^{207}Bi radioactive source obtained by directional channels 13, 15, and 17 in red.

Figure 5 also shows the multichannel energy spectra of radioactive sources ^{133}Ba and ^{241}Am obtained from directional channels 13, 15, and 17 in blue and black, respectively. Multiple characteristic energy peaks can be identified in the multichannel energy spectra of radioactive sources measured in the three directional channels, including six gamma-ray peaks at 59.6 keV, 74.2 keV, 81 keV, 276 keV, 303 keV, and 356 keV, and one internal conversion electron peak at 481.6 keV.

Through Gaussian fitting, the channel number corresponding to the peak energy of each characteristic peak can be obtained. By performing linear fitting on the distribution of characteristic peak energies and channel numbers obtained from each directional channel, the energy response equation can be obtained, as shown in Formula (1):

$$E = E_{\mathrm{perCh}} \times \mathrm{Ch} + E_0, \tag{1}$$

where E is the energy deposited by the particle in the detector (approximately equal to the total energy of the nonpenetrating electrons), Ch is the analog-digital converter (ADC) channel number, E_0 is the energy value corresponding to an ADC channel number of 0, and E_{perCh} is the channel width, which is the energy corresponding to each ADC channel number, measured in kilo electron volts per channel. The linearity is calculated using Formula (2):

$$\mathrm{Linearity} = \Delta E_{\mathrm{max}}/E_{\mathrm{max}} \times 100\%, \tag{2}$$

where ΔE_{max} is the maximum difference between the actual energy and the linear fitting results, and E_{max} is the full scale. The linearity characterizes nonlinear errors.

Figure 6 shows the linear fitting results of the radioactive source

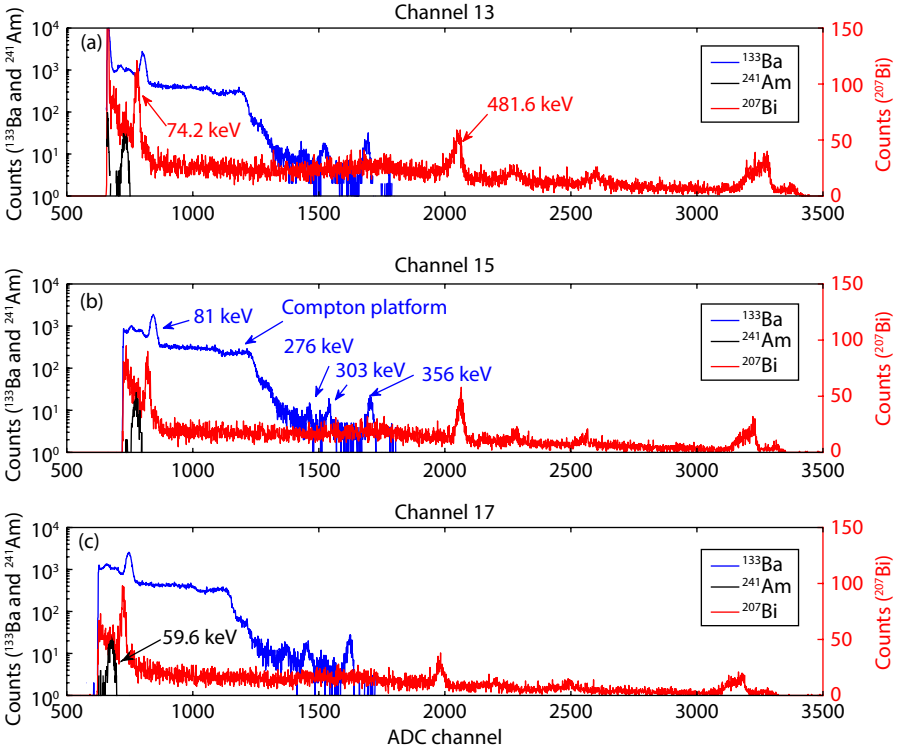

Figure 5. Multichannel energy spectra of ^{207}Bi (red), ^{133}Ba (blue), and ^{241}Am (black) measured by directional channels 13 (a), 15 (b), and 17 (c) of the cross-type medium-energy IES (adopted from Ye YG et al., 2023a).

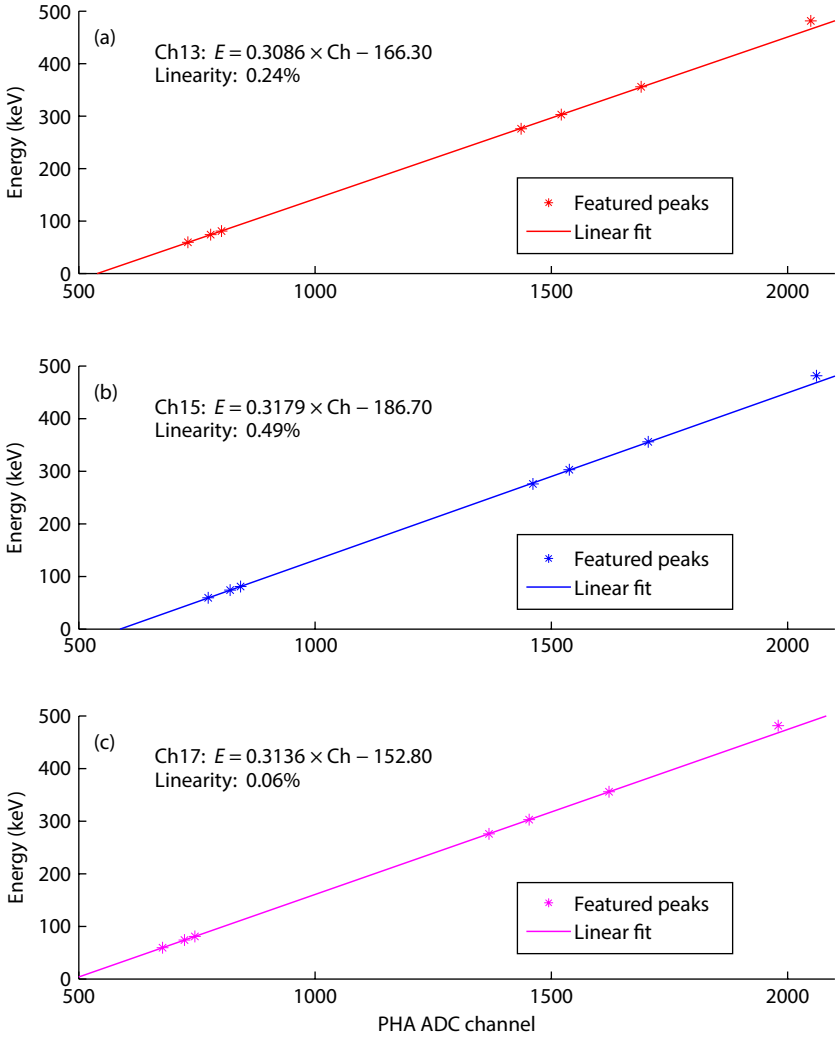

Figure 6. Linear fitting results of the radioactive source energy response measured by directional channels 13 (a), 15 (b), and 17 (c) of the cross-type medium-energy IES (adopted from Ye YG et al., 2023a).

energy response curves for directional channels 13, 15, and 17 of the cross-type medium-energy IES. From Figure 6, it can be seen that the six characteristic peaks of gamma rays measured in directional channels 13, 15, and 17 are basically coincident with the linear fitting straight line, whereas the highest energy point deviates significantly from the linear fitting straight line. The highest energy point is a characteristic peak generated by internal conversion electrons with an energy of 481.6 keV. Because the energy response test of the instrument to radioactive sources is conducted at room temperature and pressure in the laboratory, the internal conversion electrons generated by the radioactive source will lose some energy in the air. Therefore, the energy response linear fitting results of the three directional channels correspond to lower energies than the characteristic energies of the internal conversion electrons generated by the radioactive source. According to the above-mentioned results, the energy response of directional channels 13, 15, and 17 of the instrument shows good linearity (the maximum value of linearity is 0.49%). In addition, Gaussian fitting of the characteristic peak at 59.6 keV can obtain the full width at half maximum (FWHM) of the energy response peaks of the three directional channels, which are 21.0, 23.1, and 22.2 channels, respectively. Figure 6 shows the channel widths of the three directional channels: 0.3086, 0.3179, and 0.3136 keV/Ch. By multiplying the two values, we can obtain the energy resolution FWHM of the three directional channels at the characteristic peak of 59.6 keV, which are 6.48, 7.34, and 6.96 keV. This result is basically consistent with the energy resolution of the cross-type IES directional channels for single-energy single-direction electron beams measured using an electron accelerator (Ye YG et al., 2023a). In this way, by measuring the energy response of the instrument to the characteristic peak of the gamma ray from the radioactive source, its energy response to electrons can be evaluated.

3. Technical Improvement of the Imaging Probe

To achieve continuous energy spectrum detection of 10–100 keV electrons, a low-noise position-sensitive silicon semiconductor detector is required, coupled with a low-noise readout circuit. To reach a measurable electron energy lower boundary of 10 keV, the system noise (including electronic noise and inherent detector noise) must be controlled below 5 keV. While achieving 10–100 keV electron energy spectrum detection, we aimed to

retain the imaging detection capability of the small-aperture imaging probe. To achieve this goal, we planned to improve the silicon detector and amplification system based on the original pinhole imaging probe.

Currently, IESs based on the pinhole imaging technology and integrated preamplifier design can maximize the measurable electron energy range of silicon semiconductor detectors while minimizing resource consumption. For example, the medium-energy electron detector on the Fengyun-3E satellite uses a three-pixel silicon detector and an integrated preamplifier ASIC chip (RENA-3), with a measurable lower boundary of 30 keV (Ye YG et al., 2023b). The IES on the Cluster II satellites uses a silicon detector paired with an integrated switch charge amplifier chip developed by the Rutherford Laboratory to measure 20 keV electrons (Wilken et al., 1997). The Fly's Eye Energetic Particle Spectrometer (FEEPS) on the Magnetospheric Multiscale (MMS) mission uses a similar multipixel silicon detector paired with a customized integrated preamplifier ASIC chip (DAPPER) to measure ~25 keV electrons (Blake et al., 2016). As mentioned above, the current IESs based on pinhole imaging technology can measure electron energies ranging from 20 to 30 keV. Among the factors limiting the measurable energy range, in addition to the noise levels of the silicon detector and integrated preamplifier ASIC itself, is the important factor of the large physical distance between the output terminal of the silicon detector and the input terminal of the integrated preamplifier, which leads to large stray capacitance between the detector and preamplifier, greatly reducing the signal-to-noise ratio.

The technical approach of the Suprathermal Electron (STE) instrument on STEREO involves integrating the input field-effect transistor (FET) of the charge-sensitive amplifier with the silicon detector onto a single printed circuit board (PCB), with the aim of minimizing stray capacitance. Additionally, both the FET and silicon detector undergo comprehensive passive cooling to reduce electronic noise to the greatest extent possible. This unique design significantly broadens the lower boundary of electron energy for the STE, reaching approximately 2 keV (Lin RP et al., 2008). Although the detection threshold of the STE is an order of magnitude lower than that of the current IES based on the pinhole imaging technology, the STE targets interplanetary superthermal electrons. Its probe design does not utilize the pinhole imaging technology, resulting in a notably weaker imaging detection capability (with a 70° × 17° field of view in four directions) compared with the 180° × 30° field of view in nine directions achieved by IES using pinhole imaging.

We have improved the cross-type IES by drawing on the technical solutions of the STE. The principle of the improved technical route is to retain the original design of the pinhole imaging probe as much as possible, and through local improvements to the silicon detector to the integrated preamplifier system, significantly reduce the system electronic noise, thereby achieving the goal of simultaneously measuring 10–100 keV electron energy spectra in multiple directions. The following is an introduction to the improvement plan for the three-pixel detection unit.

Figure 7 shows a schematic diagram of the connection circuit between a three-pixel silicon detector and the integrated preamplifier chip RENA-3 for the cross-type IES before and after improvement. As shown in Figure 7, before improvement, the pixel signal output terminal of the silicon detector was directly connected to the input terminal of a certain channel of the integrated preamplifier ASIC through a coupling capacitor. After improvement, we added a junction FET (J-FET, model MMBF4416A) between the pixel signal output terminal of the silicon detector and the coupling capacitor. The J-FET is an N-channel J-FET (N-JFET), and its circuit constitutes a J-FET follower that reduces the impedance of the detector output signal to the order of kiloohms, significantly enhancing the signal's anti-interference ability. In addition, MMBF4416A is a J-FET with a small input capacitance, which can provide a large gain to the charge signal output by the detector, thereby improving the channel signal-to-noise ratio.

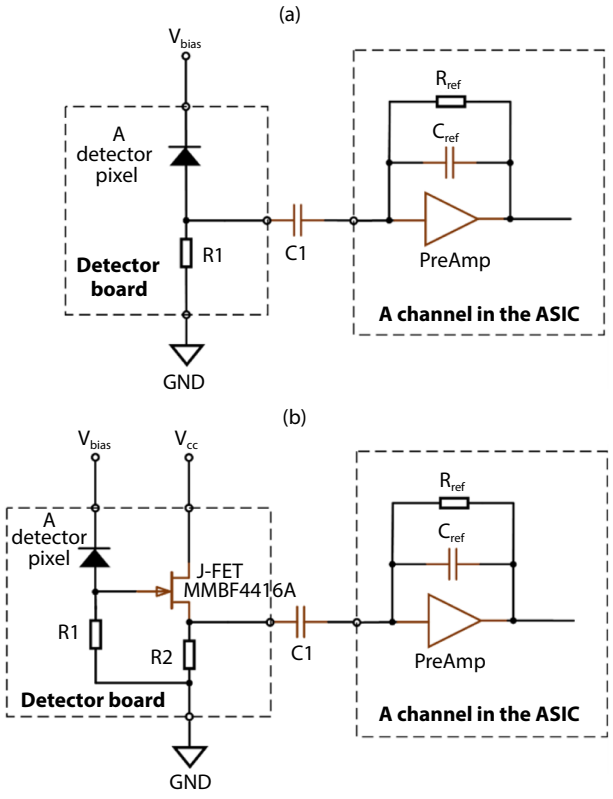

Figure 7. Schematic diagram of the connection circuit between a three-pixel silicon detector and the integrated preamplifier chip (PreAmp) RENA-3 of the cross-type IES before (a) and after (b) improvement. R1, R2 are resistors, C1 is capacitor, R_{ref} is reference resistor, C_{ref} is reference capacitor, V_{bias} is bias voltage, V_{cc} is positive supply voltage and GND is ground.

To fit the added J-FET into the limited space of the pinhole imaging probe unit, we redesigned the PCB packaging of the silicon detector and attached the bare chip of the J-FET to the PCB. The three electrodes of the J-FET were connected to the silicon detector pixels and other soldering pads through bonding wires. Figure 8 shows the improved PCB of the silicon detector and the final assembled silicon detector and protective PCB.

Figure 9 shows the cross-type IES equipped with the improved three-pixel imaging unit. As shown in the figure, we removed the

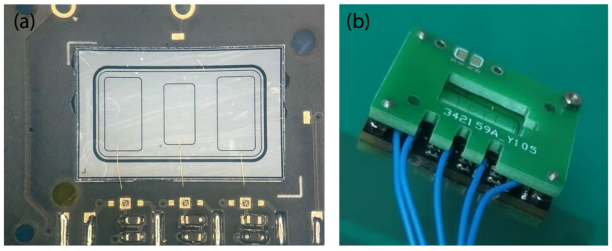

Figure 8. Printed circuit board (PCB) of the improved silicon detector (a) and the final assembled silicon detector and protective PCB (b).

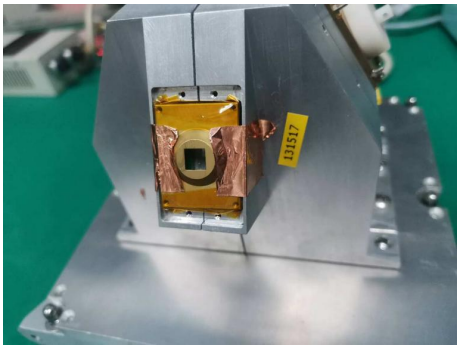

Figure 9. Cross-type IES with the improved three-pixel imaging unit installed.

pinhole structure at the front end and installed the three-pixel imaging unit in the probe structure. The reason for not installing the pinhole structure is that the flux of the radioactive source was very weak. To improve the detection efficiency of the detector, we needed to remove the small hole structure located at the front end of the imaging unit, which did not compromise the energy response measurement of the directional channel.

4. Test Results of the Improved Imaging Unit

We conducted an energy response test on the imaging unit of the improved cross-type IES by using a radioactive source. Figure 10 shows the multichannel energy spectrum of ^{133}Ba measured by the imaging unit. A comparison of Figure 5 and Figure 10 shows that the energy spectra of ^{133}Ba measured by the improved directional channels 13, 15, and 17 are significantly different from those before the improvement: (1) the lower end of the energy spectrum shows more details, including new characteristic peaks at 31 keV and 53 keV; (2) on the right side of the characteristic peak at 31 keV, a small peak (35 keV) is shown, indicating that the energy resolution of the directional channels has been greatly improved; and (3) at the high end of the energy spectrum, the Compton plateau is close to the highest channel number of the pulse height analysis (PHA), indicating that the amplification factor of the electronic system in the directional channels has increased.

Figure 11 shows the multichannel energy spectrum of ^{241}Am measured by the improved imaging unit of the cross-type IES. A comparison of Figure 5 and Figure 11 indicates that the multichannel energy spectrum of ^{241}Am measured by the improved three-direction channels shows more details at the low energy end, with the addition of three characteristic peaks at 13.8, 17.75, and 26.3 keV.

The newly detected characteristic peaks in the multichannel energy spectrum of the radioactive source can help us evaluate the directional channel performance of the improved imaging unit. Using a similar method, we investigated the linearity of the energy response of the improved imaging unit's directional channels to two types of radioactive sources, as shown in Figure 12. It can be seen that (1) the seven characteristic peak energy points of the two types of radioactive sources measured by the three direc-

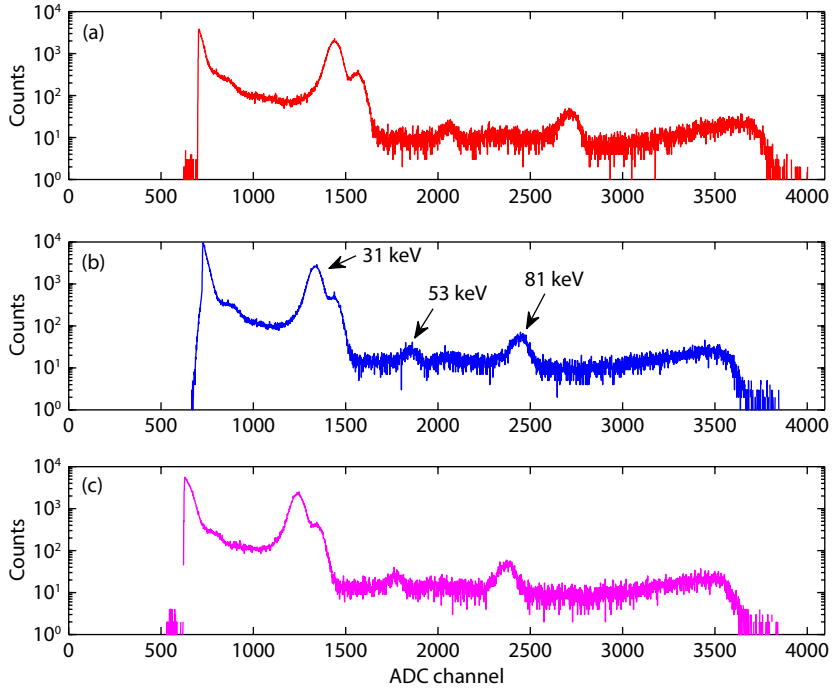

Figure 10. Multichannel energy spectrum of ^{133}Ba measured by improved cross-type IES directional channels 13 (a), 15 (b), and 17 (c).

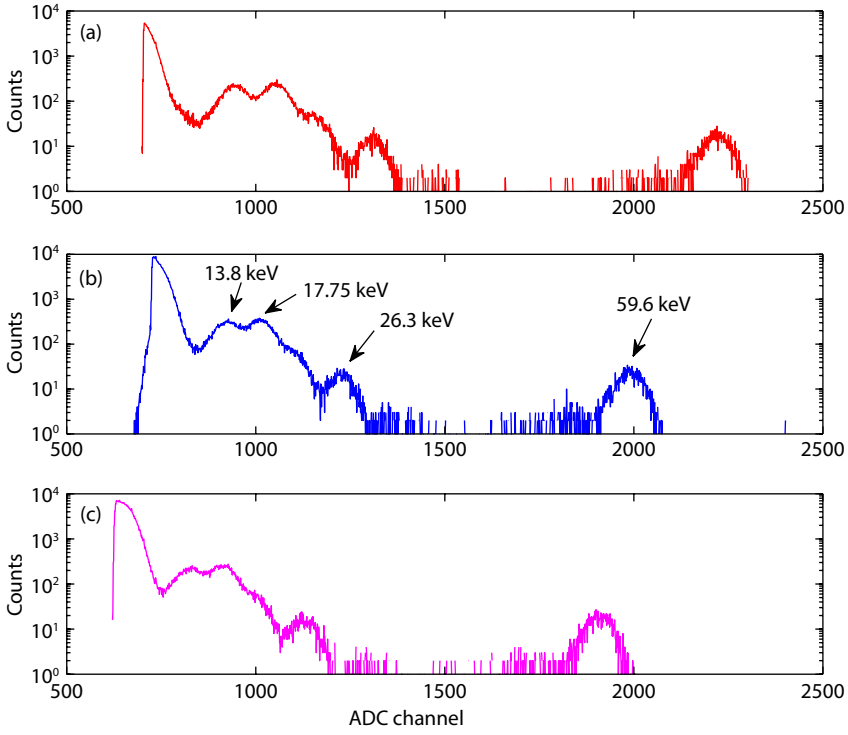

Figure 11. Multichannel energy spectrum of ^{241}Am measured by improved cross-type IES directional channels 13 (a), 15 (b), and 17 (c).

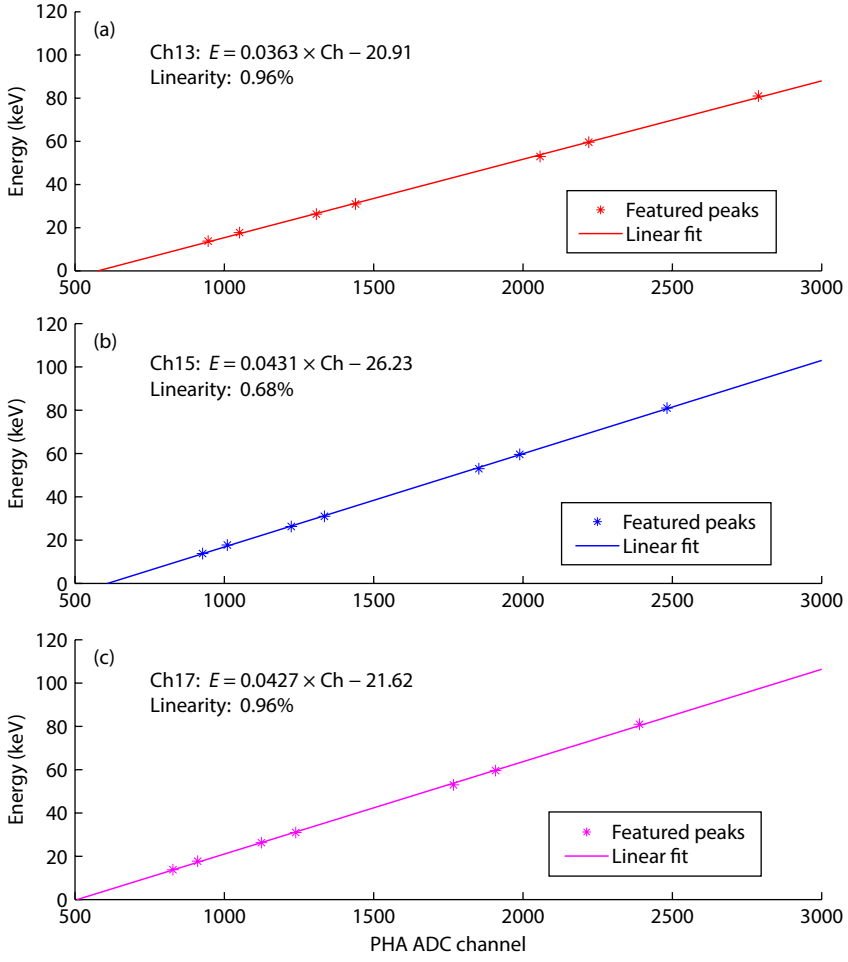

Figure 12. Linear fitting results of the radioactive source energy response measured by improved cross-type IES directional channels 13 (a), 15 (b), and 17 (c).

tional channels have good consistency with the linear fitting results, indicating that the energy response of the three directional channels has good linearity (at least in the energy range of 13.8–81 keV); and (2) from the linear fitting results of the three channels, the channel width has decreased by nearly one order of magnitude compared with before, indicating that the energy resolution of the channel may be improved.

To further confirm the measurable lower boundary of electron energy of the improved imaging unit, we conducted a background noise test using directional channel 13. That is, without adding a radioactive source, we allowed directional channel 13 to open and count background noise. We then compared the pure background noise spectrum with the multichannel energy spectrum of ^{241}Am measured by this channel. Figure 13 shows the comparison between the background noise spectrum and the multichannel energy spectrum of ^{241}Am measured by directional channel 13 of the improved imaging unit.

According to the background noise spectrum measured by directional channel 13 shown in Figure 13, the ADC channel number at the intersection point of the Gaussian fitting curve of the noise count peak and the *x*-axis is 802. Using the linear equation of energy response of directional channel 13 shown in Figure 12a, the noise threshold can be obtained as ~8.2 keV. Therefore, the improved imaging unit can detect 10 keV electrons. The FWHM channel number of the characteristic peaks of the ^{241}Am energy spectrum measured by directional channel 13 can be obtained by Gaussian fitting. Multiplying the channel width (0.03631 keV/Ch), the FWHM energies of the four characteristic peaks can be obtained as: 3.0 keV@13.8 keV, 3.1 keV@17.75 keV, 2.5 keV@26.3 keV, and 2.9 keV@59.6 keV.

From a comparison of Figure 5 and Figure 13, it can be confirmed that before the improvement, the lower boundary of electron energy that could be measured by the directional channel 13 was ~50 keV, and the energy resolution for the characteristic peak of 59.6 keV of ^{241}Am was 6.48 keV. After the improvement, the lower boundary of electron energy that could be measured by the directional channel 13 was 8.2 keV, and the energy resolution for the characteristic peak of 59.6 keV of ^{241}Am was improved by 2.9 keV. This result indicates that our improvement was effective in improving the energy resolution of the IES and expanding the lower boundary of measurable electron energy.

In this study, only the three-pixel imaging unit was redesigned to verify the improved technical solution, a design that can be applied to other imaging units. In the future, we will complete the improvement of all imaging units to achieve 10–100 keV electron energy spectrum measurement for all incident directions.

5. Conclusion

Since humanity entered the space age, decades of development in space physics have driven the demand for space exploration technology toward increasingly macro- or microscale extremes, posing formidable challenges to the capabilities of space detection instruments. Electrons within the 10–100 keV energy range constitute a vital component of energetic particles in the magnetosphere. Numerous unresolved scientific questions in magnetospheric physics stem from the inability to conduct precise observations of electrons in this energy band with high spatiotemporal and high tilt-angle resolution. Conventional space particle detectors have difficulty achieving multidirectional continuous energy spectrum measurements for electrons spanning 10–100 keV.

The medium-energy IES proposed herein, operating within the 10–100 keV range, integrates low-noise particle detection technology with pinhole imaging techniques. This enables high temporal, spatial, and energy resolution imaging detection of medium-energy electrons in the magnetosphere (10–100 keV) while achieving a compact, low-power design. Performance verification of the enhanced spectrometer was conducted through radiation source energy response testing. Test results indicate that the energy resolution of the improved medium-energy IES has increased by more than a factor of two, whereas the lower boundary of measurable electron energy has been extended from ~50 keV to 8.2 keV. The characteristic parameters of the cross-type medium-energy IES, STEREO-STE, and MEP-e are summarized in Table 1. A discussion of spectrometer design details not

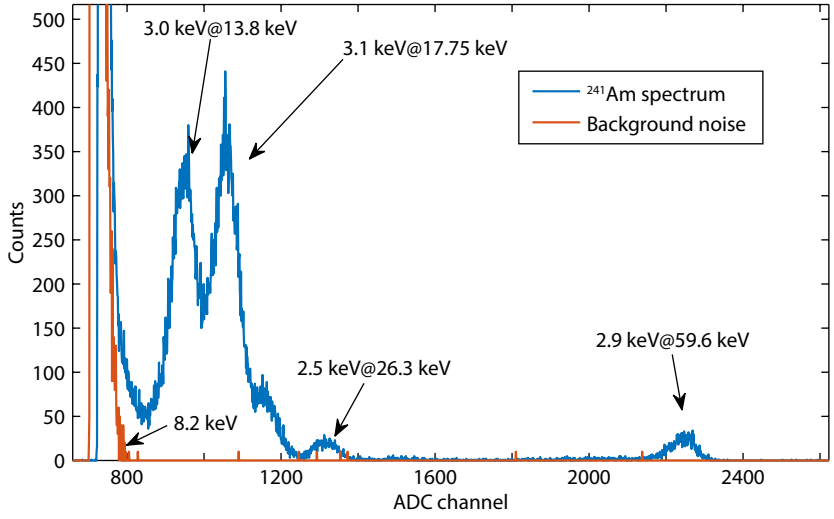

Figure 13. Background noise spectrum and ^{241}Am energy spectrum measured by the improved cross-type IES directional channel 13.

Table 1. Characteristic parameters of the cross-type medium-energy IES, STEREO-STE, and MEP-e.

Parameter	Cross-type medium-energy IES	STEREO-STE (Lin RP et al., 2008)	MEP-e (Kasahara et al., 2018)
Particles	Electron	Electron	Electron
Energy range (keV)	10–100	2–100	7–87
Energy channel (normal mode)	8 exponential channels	32 exponential channels	16 exponential channels
Energy channel (multichannel mode)	256	None	None
Field of view	$2 \times 180° \times 30°$	$70° \times 70°$ (STE-U) $80° \times 80°$ (STE-U)	$360° \times 3.5°$
Directional channels	21	4	16
Geometric factor ($cm^2 \cdot sr$)	$\sim 2.0 \times 10^{-3}$ (for each direction)[a]	0.08 (STE-U) 0.10 (STE-U)	6.6×10^{-5} (per detector)
Mass (kg)	≤3.2[b]	0.4	8.2
Size	$150 \times 150 \times 170$ mm[b]	Not mentioned	318 mm (diameter) × 395 mm
Power (W)	≤5[b]	1	21

[a]The geometric factor is the average value of nine directions. [b]Expected performance.

mentioned in this article, such as the multichannel mode, can be found in Ye YG et al. (2023a). As shown in Table 1, the upgraded medium-energy IES retains its compact size, lightweight construction, and capability for simultaneous multidirectional energy spectrum measurements. Compared with STEREO-STE and MEP-e, the new spectrometer achieves higher energy and angular resolution. Consequently, it enables imaging observations of continuous electron spectra spanning 10–100 keV, making it applicable for future space physics research and space weather applications.

Acknowledgments

This work was supported by the National Natural Science Foundation of China (Grant No. 42274225) and the International Science and Technology Cooperation Project of the Ningbo Key R&D Program (Grant No. 2024H031).

References

Blake, J. B., Fennell, J. F., Friesen, L. M., Johnson, B. M., Kolasinski, W. A., Mabry, D. J., Osborn, J. V., Penzin, S. H., Schnauss, E. R., … Hall, D. (1995). CEPPAD: Comprehensive energetic particle and pitch angle distribution experiment on POLAR. *Space Sci. Rev.*, *71*(1–4), 531–562. https://doi.org/10.1007/BF00751340

Blake, J. B., Mauk, B. H., Baker, D. N., Carranza, P., Clemmons, J. H., Craft, J., Crain, W. R. Jr., Crew, A., Dotan, Y., … Westlake, J. (2016). The Fly's Eye Energetic Particle Spectrometer (FEEPS) sensors for the magnetospheric multiscale (MMS) mission. *Space Sci. Rev.*, *199*(1–4), 309–329. https://doi.org/10.1007/s11214-015-0163-x

Evans, D. S., and Greer, M. S. (2000). *Polar orbiting environmental satellite space environment monitor-2: Instrument description and archive data documentation*. Boulder, Colorado: U.S. Dept. of Commerce.

Kasahara, S., Yokota, S., Mitani, T., Asamura, K., Hirahara, M., Shibano, Y., and Takashima, T. (2018). Medium-energy particle experiments—Electron analyzer (MEP-e) for the exploration of energization and radiation in geospace (ERG) mission. *Earth Planets Space*, *70*(1), 69. https://doi.org/10.1186/s40623-018-0847-z

Klimushkin, D. Y., Mager, P. N., Chelpanov, M. A., and Kostarev, D. V. (2021). Interaction between long-period ULF waves and charged particle in the magnetosphere: Theory and observations (overview). *Sol. Terr. Phys.*, *7*(4), 33–66. https://doi.org/10.12737/stp-74202105

Lin, R. P., Larson, D., McFadden, J., Carlson, C. W., Ergun, R. E., Anderson, K. A., Ashford, S., McCarthy, M., Parks, G. K., …Wenzel, K. P. (1996). Observation of an impulsive solar electron event extending down to ~0.5 keV energy. *Geophys. Res. Lett.*, *23*(10), 1211–1214. https://doi.org/10.1029/96GL00710

Lin, R. P., Curtis, D. W., Larson, D. E., Luhmann, J. G., McBride, S. E., Maier, M. R., Moreau, T., Tindall, C. S., Turin, P., and Wang, L. H. (2008). The STEREO IMPACT suprathermal electron (STE) instrument. *Space Sci. Rev.*, *136*(1–4), 241–255. https://doi.org/10.1007/s11214-008-9330-7

Liu, Z. Y., Zong, Q. G., Hao, Y. X., Liu, Y., and Chen, X. R. (2018). The radial propagation characteristics of the injection front: A statistical study based on BD-IES and van Allen Probes observations. *J. Geophys. Res.: Space Phys.*, *123*(3), 1927–1937. https://doi.org/10.1002/2018JA025185

Luhmann, J. G., Curtis, D. W., Schroeder, P., McCauley, J., Lin, R. P., Larson, D. E., Bale, S. D., Sauvaud, J. A., Aoustin, C., … Gosling, J. T. (2008). STEREO IMPACT investigation goals, measurements, and data products overview. *Space Sci. Rev.*, *136*(1–4), 117–184. https://doi.org/10.1007/s11214-007-9170-x

McFadden, J. P., Carlson, C. W., Larson, D., Ludlam, M., Abiad, R., Elliott, B., Turin, P., Marckwordt, M., and Angelopoulos, V. (2009). The THEMIS ESA plasma instrument and in-flight calibration. In J. L. Burch, et al. (Eds.), *The THEMIS Mission*. New York: Springer. https://doi.org/10.1007/978-0-387-89820-9_13

Rodríguez-Pacheco, J., Wimmer-Schweingruber, R. F., Mason, G. M., Ho, G. C., Sánchez-Prieto, S., Prieto, M., Martín, C., Seifert, H., Andrews, G. B., … Zong, Q. (2020). The energetic particle detector: Energetic particle instrument suite for the Solar Orbiter mission. *Astron. Astrophys.*, *642*, A7. https://doi.org/10.1051/0004-6361/201935287

Summers, D., Thorne, R. M., and Xiao, F. L. (1998). Relativistic theory of wave-particle resonant diffusion with application to electron acceleration in the magnetosphere. *J. Geophys. Res.: Space Phys.*, *103*(A9), 20487–20500. https://doi.org/10.1029/98JA01740

Thorne, R. M. (2010). Radiation belt dynamics: The importance of wave-particle interactions. *Geophys. Res. Lett.*, *37*(22), L22107. https://doi.org/10.1029/2010GL044990

Thorne, R. M., Li, W., Ni, B., Ma, Q., Bortnik, J., Chen, L., Baker, D. N., Spence, H. E., Reeves, G. D., … Kanekal, S. G. (2013). Rapid local acceleration of relativistic radiation-belt electrons by magnetospheric chorus. *Nature*, *504*(7480), 411–414. https://doi.org/10.1038/nature12889

Tindall, C. S., Palaio, N. P., Ludewigt, B. A., Holland, S. E., Larson, D. E., Curtis, D. W., McBride, S. E., Moreau, T., Lin, R. P., and Angelopoulos, V. (2008). Silicon detectors for low energy particle detection. *IEEE Trans. Nucl. Sci.*, *55*(2), 797–801. https://doi.org/10.1109/TNS.2008.918527

Tumer, T. O., Cajipe, V. B., Clajus, M., Hayakawa, S., and Volkovskii, A. (2006). Multi-channel front-end readout IC for position sensitive solid-state

detectors. In *Proceedings of 2006 IEEE Nuclear Science Symposium Conference Record* (pp. 384–388). San Diego, California: IEEE. https://doi.org/10.1109/NSSMIC.2006.356181

Wilken, B., Axford, W. I., Daglis, I., Daly, P., Güttler, W., Ip, W. H., Korth, A., Kremser, G., Livi, S., … Ullaland, S. (1997). RAPID–The imaging energetic particle spectrometer on Cluster. *Space Sci. Rev.*, *79*(1–2), 399–473. https://doi.org/10.1023/A:1004994202296

Ye, Y. G., Zou, H., Zong, Q. G., Chen, H. F., Zou, J. Q., Shi, W. H., Yu, X. Q., Zhong, W. Y., Wang, Y. F., … Hao, X. Y. (2021). Energetic electron detection packages on board Chinese navigation satellites in MEO. *Earth Planet. Phys.*, *5*(2), 158–179. https://doi.org/10.26464/epp2021021

Ye, Y. G., Zou, H., Wang, Y. F., Qin, J. F., Shi, W. H., Zou, J. Q., Zhong, W. Y., Zong, Q. G., and Fu, S. Y. (2023a). A cross-type imaging electron spectrometer. *Sci. China Technol. Sci.*, *66*(3), 641–653. https://doi.org/10.1007/s11431-022-2103-7

Ye, Y. G., Li, J. W., Huang, C., Zou, H., Zong, Q. G., Zhang, X. X., Wang, J. S., Liu, Y., Wang, Y. F., … Shao, S. P. (2023b). Medium-energy electron detector onboard the FY-3E satellite. *Space Wea.*, *21*(3), e2022SW003241. https://doi.org/10.1029/2022SW003241

Ye, Y. G., Liu, Y., Zou, H., Zong, Q. G., Chen, J. L., Yu, X. Q., Shi, W. H., Ou, J. M., Liu, J. B., … Suo, L. (2024). Medium-energy electron spectrometers on Macao Science Satellite-1. *Sci. China Technol. Sci.*, *67*(11), 3324–3343. https://doi.org/10.1007/s11431-023-2676-6

Zong, Q. G., Hao, Y. X., Zou, H., Fu, S. Y., Zhou, X. Z., Ren, J., Wang, L. H., Yuan, C. J., Liu, Z. Y., … Wang, Y. F. (2016). Radial propagation of magnetospheric substorm-injected energetic electrons observed using a BD-IES instrument and Van Allen Probes. *Sci. China Earth Sci.*, *59*(7), 1508–1516. https://doi.org/10.1007/s11430-016-0039-0

Zong, Q. G., Rankin, R., and Zhou, X. Z. (2017). The interaction of ultra-low-frequency pc3–5 waves with charged particles in Earth's magnetosphere. *Rev. Mod. Plasma Phys.*, *1*(1), 10. https://doi.org/10.1007/s41614-017-0011-4

Zong, Q. G. (2022). Magnetospheric response to solar wind forcing: Ultra-low-frequency wave–particle interaction perspective. *Ann. Geophys.*, *40*(1), 121–150. https://doi.org/10.5194/angeo-40-121-2022

Zou, H., Ye, Y. G., Zong, Q. G., Chen, H. F., Zou, J. Q., Chen, J., Shi, W. H., Yu, X. Q., Zhong, W. Y., … Zhang, X. X. (2018). Imaging energetic electron spectrometer onboard a Chinese navigation satellite in the inclined GEO orbit. *Sci. China Technol. Sci.*, *61*(12), 1845–1865. https://doi.org/10.1007/s11431-018-9321-7